
GLOBAL COUNTERFACTUAL DIRECTIONS

Bartłomiej Sobieski
Warsaw University of Technology
Warsaw, Poland

Przemysław Biecek
University of Warsaw
Warsaw, Poland

ABSTRACT

Despite increasing progress in development of methods for generating visual counterfactual explanations, especially with the recent rise of Denoising Diffusion Probabilistic Models, previous works consider them as an entirely local technique. In this work, we take the first step at globalizing them. Specifically, we discover that the latent space of Diffusion Autoencoders encodes the inference process of a given classifier in the form of global directions. We propose a novel proxy-based approach that discovers two types of these directions with the use of only *single* image in an *entirely black-box* manner. Precisely, g-directions allow for flipping the decision of a given classifier on an *entire* dataset of images, while h-directions further increase the diversity of explanations. We refer to them in general as Global Counterfactual Directions (GCDs). Moreover, we show that GCDs can be naturally combined with Latent Integrated Gradients resulting in a new black-box attribution method, while simultaneously enhancing the understanding of counterfactual explanations. We validate our approach on existing benchmarks and show that it generalizes to real-world use-cases.

Keywords Counterfactual explanations · Black-box method · Diffusion models · Representation understanding

1 Introduction

The ongoing revolution caused by the emergence of artificial intelligence algorithms with human-like performance creates a natural demand for explaining their inner workings. This trend is visible in various domains ranging from art and games [1, 2] to medical and healthcare applications [3, 4] to autonomous driving and human-like dialogue [5, 6]. Machine learning models can be explained using a number of methods [7] which form the Explainable Artificial Intelligence domain. *Counterfactual explanations* (CEs) [8, 9] aim to answer the fundamental question behind the reasoning process of a given model: for a given instance, what is the minimal meaningful modification that results in changing the model’s outcome? This type of local explanation stands at the highest level of Pearl’s causality ladder [10] as they help humans in identifying the *cause-effect* relations of the model’s decision and its input.

In computer vision, constructing visual CEs [11] for classification models has been a rapidly growing research direction [12]. Current state-of-the-art (SOTA) approaches [13, 14, 15, 16] utilize the framework of diffusion models (DMs) [17, 18, 19], which generate data by progressive denoising. Importantly, these methods assume *white-box* access to the model of interest. This means that they can fully exploit model’s internal structure and differentiability. Much less attention was paid to *black-box* methods that assume access to only input-outputs pairs of the target classifier [20]. Generating CEs in a black-box scenario poses a much more challenging task as the available signal is considerably weaker, making it difficult to perform *targeted* changes in the image and influence only relevant areas. Developing black-box methods is essential, as they relate to many practical scenarios, e.g. when the model of interest is available only through an API.

Current SOTA methods for generating visual CEs often do not possess any internal mechanisms that would indicate which changes in the image *actually* influenced the classifier’s decision and which were less relevant or could be omitted. To do that, they would have to resort to other approaches like attribution methods. This limitation is greatly emphasized in black-box scenarios, where only model-agnostic methods could be used to provide such information, and where introducing only relevant changes is much more challenging.

CEs are generated independently for each image. While some approaches exist that aim to find connections between them by e.g. influencing a specific attribute of different images [21], CEs are mostly considered as an entirely local

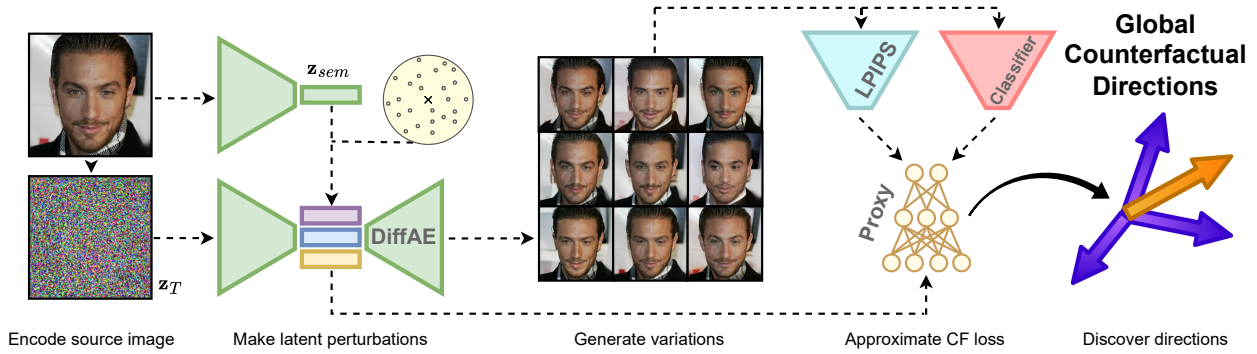


Figure 1: Conceptual summary of the introduced method. We first encode the source image and create local perturbations of its semantic latent representation. By generating the images from these perturbations and putting them through LPIPS and the target classifier, we obtain training data for the proxy network which locally approximates the counterfactual loss. Using a trained proxy, we discover g- and h-directions, which we term Global Counterfactual Directions, as single direction allows for generating counterfactual explanations for the entire dataset of images.

technique. We argue that showing their *global* properties, especially in a black-box scenario, would be highly beneficial for future research directions and development of novel methods.

Considering the above limitations, we introduce Global Counterfactual Directions (GCDs) and make the following contributions:

1. Our method discovers directions in the semantic latent space of a Diffusion Autoencoder (DiffAE) that are able to flip the classifier’s decision *globally*, i.e. for an entire dataset of images. We divide them into gradient-based and hessian-based. Moreover, our method requires only a single image to find them and is entirely black-box.
2. GCDs can be naturally combined with Latent Integrated Gradients (LIG) forming a novel black-box attribution method. This enhances the understanding of the obtained CEs by highlighting changes that influenced the classifier’s decision and disregarding irrelevant input modifications.
3. GCDs outperform current SOTA black-box method on CelebA-HQ despite extracting information about the classifier from only single image, no assumptions about classifier’s training data availability and a much smaller model. They also achieve very competitive performance in comparison to white-box methods on both CelebA and CelebA-HQ. In addition, the properties of GCDs transfer to real-world use-cases, which we demonstrate on a challenging CheXpert benchmark.

For a conceptual summary of our approach, see 1.

2 Related work

Our work focuses on the task of constructing visual CEs for classification models. This type of local explanation, i.e. performed for a single observation, aims at explaining the decision of a given classifier by modifying the input image so that this decision gets changed. For example, the model changes its prediction from *fish* to *bird* when feathers are added to the original image. Contrary to adversarial attacks [22, 23], CEs aim at introducing minimal *semantic* change instead of noisy perturbations. Construction of visual CEs has emerged as an independent research direction in recent years [12, 24, 25, 26, 27, 28].

A number of works utilizes generative models, such as VAEs [29] or GANs [30], to properly modify the image to change classifier’s decision [31, 32, 33, 34, 35, 36]. Lately, due to its exceptional capabilities in image generation tasks, diffusion models (DMs) emerged as the SOTA in generating CEs. DiME [14], the first approach that applied DMs for this task, guides the generative process using classifier’s gradients. ACE [13] combines DMs with adversarial attacks to inpaint semantic changes. This line of research is under active development [16, 37]. Importantly, these methods treat the target classifier as a *white-box*, i.e. assuming full access to internal structure and exploiting its differentiability. These provide important knowledge about specific regions of the image that should be modified.

Despite their effectiveness, white-box methods are not applicable in many practical scenarios, e.g. when the model can be accessed exclusively via an API so that only input-output pairs are available. In recent works, much less attention has

been paid to this *black-box* scenario. Assuming access to classifier’s training data availability, TiME [20] uses Stable Diffusion [1], a highly parameterized text-to-image foundation model, in a black-box manner. Other approaches put more focus on analyzing the dataset and its biases to create distributional shifts [38, 39, 40]. They do not specifically consider what the target model has learned, only that it changes its decision when faced with images far from training data distribution. In this paper, we aim at advancing the state of black-box methods while showing that a single image suffices to extract the knowledge about the target model required to produce CEs.

Since CEs are a local explanation technique, most previous works treat them independently between different images. In this context, the work StyleEX [21] can be considered an exception. They first train a GAN that incorporates the knowledge about the classifier of interest in its latent space in a white-box manner. They then detect classifier-specific directions in GAN’s latent space responsible for changing specific attributes in images which influence the classifier’s output. It is shown that in some cases a set of such directions results in flipping the classifier’s decision for a large fraction of images.

Since the emergence of DMs, many papers focused on analyzing their latent space, e.g. to discover semantically meaningful directions or utilize it for downstream tasks [41, 42, 43, 44, 45, 46]. While these works contribute significant scientific value, they make no connection with CEs generation or other model’s explainability in general. In this work, we implicitly contribute to this research direction while focusing on the given classifier’s interpretability. Specifically, we focus on analyzing the latent space of DiffAE [47], a subclass of DMs suited for representation learning [48, 49], which decomposes its latent space into a high-dimensional part responsible for stochastic details, and the compressed one with rich semantic knowledge.

In addition, our work addresses the topic of attribution methods for classification models [50, 51, 52, 53]. Contrary to CEs, these approaches produce a heatmap over the original image indicating regions that influence the classifier’s decision. In a white-box setting, Integrated Gradients (IG) [54] method was one of the first mathematically-grounded approaches, producing the attribution map with the use of a *baseline* image. Choosing a proper baseline sparked great interest, resulting in a number of works arguing about the optimal choice [55, 56, 57]. While the original work uses a black image, the authors of MedXGAN [58] suggested that the baseline should be a semantically plausible image to avoid evaluating the classifier on out-of-distribution data, a proposition upon which we build in this work.

3 Background

3.1 Visual counterfactual explanations

Visual CEs aim at changing the classifier’s prediction, e.g. from old to young when classifying a person’s age, by introducing only semantically plausible changes to the image. Typically, this problem is formulated as minimizing the following *counterfactual loss* (CF) function:

$$\mathcal{L}_{CF}(\tilde{\mathbf{x}}) = f(\tilde{\mathbf{x}}) + \lambda \cdot s(\mathbf{x}, \tilde{\mathbf{x}}), \quad (1)$$

where \mathbf{x} denotes the original image, $\tilde{\mathbf{x}}$ the CE proposal, f the classifier of interest and $s(\mathbf{x}, \tilde{\mathbf{x}})$ a measure of perceptual distance between \mathbf{x} and $\tilde{\mathbf{x}}$. For simplicity, we assume that f returns a positive score for \mathbf{x} , which indicates a positive class (e.g. young), and we aim to minimize that score with $\tilde{\mathbf{x}}$ so that it becomes negative, i.e. f predicts a negative class (e.g. old), while keeping $s(\mathbf{x}, \tilde{\mathbf{x}})$ as small as possible. The λ parameter accounts for the trade-off between semantic similarity and the change in classifier’s score. For the s function, the research community has widely adopted the LPIPS [59] metric, which was shown to strongly resemble how humans perceive semantic similarity between images.

3.2 Diffusion models

Denoising Diffusion Probabilistic Models (DDPMs) [18] and their further enhancements have revolutionized generative image modelling, exceeding the performance of GANs and allowing for various mechanisms of controlling the generation process [60]. These models are trained to sequentially remove noise from a corrupted image, typically using a U-Net architecture [61], so that after a number of forward passes through the network a clean image is obtained. Specifically, images are first mapped to noise with a *forward process*, while the neural network aims at reversing this mapping, i.e. it approximates the *reverse process*. Originally, both processes are formulated as *stochastic* processes, making it difficult to precisely reconstruct a given image from noise. Denoising Diffusion Implicit Models (DDIM) [62] overcome this issue by deriving a family of parameterized processes which turn out to be also solved by a pretrained DDPM. Concretely, DDIM refers to a particular process from this family which is *deterministic*. Hence, it allows for mapping a given image to noise and then retrieving it with great accuracy using a pretrained model.

DMs operate in the space of the same dimensionality as input images. This makes their original formulation not particularly suitable for various tasks specific to e.g. representation learning [48, 49]. While some works explore the

capabilities of sequences of representations that appear in the underlying neural network [41, 42, 43, 44, 45, 46], DiffAE attempts to condition a DM with additional semantically rich signal coming from a *semantic encoder* E_ϕ . Concretely, they perform a joint training of E_ϕ with the denoising network ϵ_θ . This is done by first encoding the original image \mathbf{x} with E_ϕ to a low-dimensional vector $\mathbf{z}_{sem} = E_\phi(\mathbf{x})$. The image is then corrupted with gaussian noise ϵ_t to produce \mathbf{x}_t , a noised version of \mathbf{x} at timestep t of the forward process. The denoising network ϵ_θ then receives \mathbf{x}_t as input together with the additional conditioning signal \mathbf{z}_{sem} and is trained to approximate the added noise.

A trained DiffAE is able to accurately reconstruct a given image as attaching an additional encoder to a default DM does not violate any assumptions of both DDPM and DDIM. More specifically, to reconstruct \mathbf{x} , it is first passed through E_ϕ to obtain \mathbf{z}_{sem} . Next, the denoising network ϵ_θ is conditioned with \mathbf{z}_{sem} to obtain \mathbf{z}_T , i.e. the noised version of \mathbf{x} at the last timestep T of the forward process, by following the DDIM update rule. Both \mathbf{z}_{sem} and \mathbf{z}_T can then be used to reconstruct \mathbf{x} using the reverse process. We denote the final output of this procedure (the reconstruction of \mathbf{x}) as $DAE(\mathbf{z}_{sem}, \mathbf{z}_T)$. The authors show that the *semantic latent space* represented by \mathbf{z}_{sem} possesses *global editing directions* [47]. Moving along such direction influences a specific semantic attribute in every image, such as adding or removing moustache.

3.3 Integrated Gradients

IG stands as one of the first attribution methods for differentiable models with solid mathematical foundations. For a given image \mathbf{x} , it assumes access to a baseline image \mathbf{x}' , i.e. an image for which the classifier’s prediction is close to zero. In the original formulation, a black image is chosen, as it often results in such prediction. Many works argue about a proper choice of the baseline, emphasizing that a black image is not an optimal choice. The MedXGAN method proposes to generate a semantically plausible baseline \mathbf{x}' by editing \mathbf{x} with a GAN trained together with a classifier in a white-box manner. Such baseline can be understood as a CE with additional constraint that the classifier’s output is approximately 0. By interpolating between the latent representations of \mathbf{x} and \mathbf{x}' in the GAN’s latent space, they obtain a sequence of images $\{\mathbf{x}_k\}_{k=1}^m$. These are used to approximate the attribution of the i -th pixel, resulting in Latent Integrated Gradients (LIG) method. Specifically, the attribution of the i -th pixel is computed as follows:

$$LIG_i(\mathbf{x}) = \frac{1}{m}(\mathbf{x}_i - \mathbf{x}'_i) \sum_{k=1}^m \nabla_{\mathbf{x}_k} f(\mathbf{x}_k). \quad (2)$$

4 Method

As shown in the original DiffAE paper [47], the capabilities of \mathbf{z}_T for image editing purposes are limited. Varying it while keeping \mathbf{z}_{sem} constant affects only small details such as earrings or the arrangement of individual hair strands. In addition, \mathbf{z}_T is high-dimensional (the same as the input image) so any optimization procedure involving it would be costly. Because of that, we shift our focus to the semantic code \mathbf{z}_{sem} which is shaped as a flat vector of short length (typically 512) and was shown to contain most of the semantic information in a compressed manner in the form of directions. To edit a given image \mathbf{x} with \mathbf{z}_{sem} , we must therefore find a specific direction \mathbf{d} that meets our needs and move \mathbf{z}_{sem} along it. Specifically, we first obtain \mathbf{z}_{sem} with the encoder, then compute \mathbf{z}_T using \mathbf{z}_{sem} and DDIM, move \mathbf{z}_{sem} along \mathbf{d} to obtain $\tilde{\mathbf{z}}_{sem} = \mathbf{z}_{sem} + \alpha \mathbf{d}$ for some scalar α and decode the modified image $\tilde{\mathbf{x}} = DAE(\tilde{\mathbf{z}}_{sem}, \mathbf{z}_T)$. As we are interested in finding $\tilde{\mathbf{x}}$ that minimizes the counterfactual loss from 1, the only remaining question is *how* to find a proper direction \mathbf{d} and scalar α . A naive approach would be to simply compute the gradient of $\mathcal{L}_{CF}(\tilde{\mathbf{x}})$ with respect to \mathbf{z}_{sem} . However, this approach would violate the assumption that f is a black-box model for which only input-output pairs are available, and differentiate through the classifier as well as a long sequence of forward passes through the denoising network. We have to therefore resort to a different approach.

Let \mathbf{x} be an arbitrary image which we will relate to as the *source image*. We assume that \mathbf{z}_{sem} is its latent code obtained through the encoder while \mathbf{z}_T is computed as mentioned above and kept fixed. To find a proper direction \mathbf{d} and scalar α that will result in $\tilde{\mathbf{x}} = \mathbf{x} + \alpha \mathbf{d}$ being a CE, we propose to locally approximate the relationship between \mathbf{z}_{sem} and $\mathcal{L}_{CF}(\tilde{\mathbf{x}})$. Note that any dependency between \mathcal{L}_{CF} and $\tilde{\mathbf{x}}$ is contained within \mathbf{z}_{sem} as long as \mathbf{z}_T is kept fixed. To obtain this approximation, we introduce a *proxy network* p_ψ . In practice, p_ψ is a lightweight MLP network consisting of 5 linear layers and sigmoid activations with input layer size equal to the length of \mathbf{z}_{sem} and the output layer of length 2. The first output p_ψ^f accounts for approximating $f(\tilde{\mathbf{x}})$ while the second one p_ψ^s for $s(\mathbf{x}, \tilde{\mathbf{x}})$. Combining these outputs with λ from 1 results in approximating the counterfactual loss. To train p_ψ , we first sample a set of δ values from uniform distribution on an n -ball of radius r . Here, n is equal to the length of \mathbf{z}_{sem} and r a hyperparameter. Next, we add δ to \mathbf{z}_{sem} to create local perturbations $\tilde{\mathbf{z}}_{sem} = \mathbf{z}_{sem} + \delta$. At last, we generate $\tilde{\mathbf{x}} = DAE(\tilde{\mathbf{z}}_{sem}, \mathbf{z}_T)$. By computing

$f(\tilde{\mathbf{x}})$ and $s(\mathbf{x}, \tilde{\mathbf{x}})$, we obtain the training data for p_{ψ} in the form of $D = \{\tilde{\mathbf{z}}, (f(\tilde{\mathbf{x}}), s(\mathbf{x}, \tilde{\mathbf{x}}))\}$. We include pseudocode and an extensive description of proxy training in the Appendix.

We propose to utilize a trained proxy network to obtain *counterfactual directions*, i.e. directions that minimize the counterfactual loss \mathcal{L}_{CF} , as follows. Using automatic differentiation, we first compute

$$\mathbf{d}_g = \nabla_{\mathbf{z}_{sem}} \left(p_{\psi}^f(\mathbf{z}_{sem}) + \lambda p_{\psi}^s(\mathbf{z}_{sem}) \right). \quad (3)$$

We term \mathbf{d}_g as *g-direction*, which is the gradient of the approximate counterfactual loss with respect to \mathbf{z}_{sem} . Therefore, $-\mathbf{d}_g$ should approximately indicate the direction of the steepest descent of the CF loss. However, even if effective, \mathbf{d}_g constitutes only a single counterfactual direction for \mathbf{x} . To obtain more directions, we propose to additionally compute the hessian \mathbf{H} of the approximate counterfactual loss:

$$\mathbf{H} = \nabla_{\mathbf{z}_{sem}}^2 \left(p_{\psi}^f(\mathbf{z}_{sem}) + \lambda p_{\psi}^s(\mathbf{z}_{sem}) \right). \quad (4)$$

We then compute its eigenvectors $\{\mathbf{d}_h^i\}_{i=1}^n$ and sort them according to the magnitude (absolute value) of their eigenvalues. These indicate the directions in which the approximate CF loss varies locally most. We refer to them as *h-directions*. They are orthogonal by definition, which should result in influencing different semantic attributes. For more details regarding the h-directions derivation, please refer to the Appendix.

To find a proper value of α for a given direction \mathbf{d} , we propose a simple line search procedure, i.e.

$$\alpha = \arg \min_k (\mathcal{L}_{CF}(DAE(\mathbf{z}_{sem} + \alpha_k \mathbf{d}, \mathbf{z}_T))), \quad (5)$$

where k indexes a set of uniformly spaced values $\{\alpha_k\}_k$. In practice, we can perform the line search using a single batch, exploiting the parallel computation on a GPU.

We have introduced a theoretically supported algorithm for obtaining a single g-direction and a set of h-directions, and how to move along them so that the resulting image should end up being a CE. Importantly, this procedure is limited to a single source image \mathbf{x} . However, through the experimental evaluation, we empirically prove that g- and h-directions are *transferable* across an entire dataset of images. That is, they are able to flip the classifier’s decision *globally* even though they were found using only single image. Moreover, we show that their *globality* behaves in a principled way, with the g-direction being *the most global*, and the h-directions being decreasingly *less global* while increasing the diversity of explanations. We refer to both g- and h-directions as Global Counterfactual Directions (GCDs).

GCDs can be also used to extend the existing techniques for model explanation. One such case is the LIG method which builds upon IG, where the attribution map is built by integrating over a sequence of images beginning from the so-called baseline \mathbf{x}' – by default being a black image for IG. LIG requires finding a semantically plausible baseline \mathbf{x}' and interpolating between it and the original \mathbf{x} in a semantic latent space (see 2). Contrary to original formulation of LIG, GCDs allow to do that in an entirely black-box manner with no classifier-specific training of the generative model and per-image optimization except line search. These properties eliminate any white-box assumptions from the baseline search and interpolation. However, standard IG and LIG also exploit them when computing derivatives inside the integral. To extend LIG to an entirely black-box approach, we propose to approximate the derivatives using the finite difference method [63]. This way, GCDs lead to a novel black-box attribution method, which we term Black-Box Latent Integrated Gradients (BB-LIG). Specifically, we compute the attribution of the i -th pixel as

$$BB-LIG_i(\mathbf{x}) = \frac{1}{m} (\mathbf{x}_i - \mathbf{x}'_i) \sum_{k=1}^m \frac{f(\tilde{\mathbf{x}}_{k+1}) - f(\tilde{\mathbf{x}}_k)}{\tilde{\mathbf{x}}_{k+1} - \tilde{\mathbf{x}}_k}, \quad (6)$$

where $\tilde{\mathbf{x}}_k = DAE(\mathbf{z}_{sem} + \alpha_k \mathbf{d}, \mathbf{z}_T)$ with \mathbf{d} being a GCD and \mathbf{x}_i denoting the value of the i -th pixel. For the case when $\tilde{\mathbf{x}}_{k+1} - \tilde{\mathbf{x}}_k = 0$, we simply set the derivative’s approximation to zero. It is an intuitive choice since no change in the pixel’s value should be treated as not influencing the classifier’s prediction. BB-LIG also allows for full utilization of the used resources, as finding any CE in our framework requires generating a sequence of images with line search. Overall, by computing the attributions with BB-LIG, we are able to enhance the obtained CEs with an indication of most important regions while simultaneously getting a better insight at the classifier’s decision-making process. We demonstrate that from a practical point of view through the experimental evaluation.

5 Experiments

To perform a thorough and fair comparison with recent approaches to generating CEs [14, 13, 34, 33, 20], we base our experimental evaluation on two most popular benchmarks of face images: CelebA [64] and CelebA-HQ [65]. The former consists of around 200,000 images of 128×128 resolution, while the latter of 30,000 images with 256×256 resolution. Following previous works, we use DenseNet [66] from [14] for CelebA and from [34] for CelebA-HQ as the classifiers of interest. For both datasets, we generate CEs for the *smile* and *age* classes. We also evaluate our method on CheXpert [67] - a challenging benchmark of around 200,000 X-ray 224×224 resolution images. We use the DenseNet classifier from [68] as the model of interest. We point out that a pretrained DiffAE is not available for any of those datasets. For CelebA-HQ, we use the original checkpoint trained on the FFHQ-256 dataset [69]. For CelebA and CheXpert, we train DiffAE from scratch. In terms of quantitative evaluation, we follow the work of [13]. For information regarding the used hyperparameters, description of the used metrics, additional ablation studies and pseudocode, please refer to the Appendix.

We begin our experimental evaluation by comparing the performance obtained with g-directions to current SOTA approaches. Next, we demonstrate the effectiveness of the h-directions and their role as a complement to g-directions. We finish with an evaluation of BB-LIG. For extended results and more visual examples, please refer to the Appendix.

Table 1: Evaluation of g-directions on CelebA datasets. Rows correspond to different methods of either white- or black-box type (separated by dashed line), and each segment to a dataset-class pair. Columns indicate metrics with \downarrow meaning lower is better and \uparrow that higher is better. Results of methods other than GCD are extracted from TiME [20] and ACE [13].

Dataset		CelebA-HQ								
Class		Age								
Method	Metric	FID(\downarrow)	sFID(\downarrow)	FVA(\uparrow)	FS(\uparrow)	MNAC(\downarrow)	CD(\downarrow)	COU(\uparrow)	FR(\uparrow)	Type
	DiVE		107.5	-	32.3	-	6.76	-	-	-
STEEEX		26.8	-	96.0	-	5.63	-	-	-	White-box
DiME		18.7	27.8	95.0	0.6597	2.10	4.29	0.5615	97.0	White-box
ACE l_1		5.31	21.7	99.6	0.8085	1.53	5.40	0.3984	95.0	White-box
ACE l_2		16.4	28.2	99.6	0.7743	1.92	4.21	0.5303	95.0	White-box
TiME		20.9	32.9	79.3	0.6282	4.19	4.29	0.3124	89.9	Black-box
GCD (ours)		9.47	10.11	99.0	0.8170	4.51	3.92	0.2954	96.0	Black-box
Class		Smile								
DiVE		107.0	-	35.7	-	7.41	-	-	-	White-box
STEEEX		21.9	-	97.6	-	5.27	-	-	-	White-box
DiME		18.1	27.7	96.7	0.6729	2.63	1.82	0.6495	97.0	White-box
ACE l_1		3.21	20.2	100.0	0.8941	1.56	2.61	0.5496	95.0	White-box
ACE l_2		6.93	22.0	100.0	0.8440	1.87	2.21	0.5946	95.0	White-box
TiME		10.98	23.8	96.6	0.7896	2.97	2.32	0.6303	97.1	Black-box
GCD (ours)		7.26	7.94	99.0	0.8800	2.84	3.74	0.5077	97.5	Black-box
Dataset		CelebA								
Class		Age								
DiVE		33.8	-	98.2	-	4.58	-	-	-	White-box
STEEEX		11.8	-	97.5	-	3.44	-	-	-	White-box
DiME		4.15	5.89	95.3	0.6714	3.13	3.27	0.4442	99.0	White-box
ACE l_1		1.45	4.12	99.6	0.7817	3.20	2.94	0.7176	96.2	White-box
ACE l_2		2.08	4.62	99.6	0.7971	2.94	2.82	0.5641	95.6	White-box
GCD (ours)		8.72	9.11	98.4	0.7462	3.31	3.14	0.3220	96.0	Black-box
Class		Smile								
DiVE		29.4	-	97.3	-	-	-	-	-	White-box
STEEEX		10.2	-	96.9	-	4.11	-	-	-	White-box
DiME		3.17	4.89	98.3	0.7290	3.72	2.30	0.5259	97.2	White-box
ACE l_1		1.27	3.97	99.9	0.8740	2.94	1.73	0.7828	97.6	White-box
ACE l_2		1.90	4.56	99.9	0.8670	2.77	1.56	0.6235	96.1	White-box
GCD (ours)		7.24	7.66	99.9	0.8821	2.62	3.47	0.4030	97.2	Black-box

5.1 Evaluation of g-directions

In 1, we include a quantitative comparison of CEs obtained with g-directions on the CelebA datasets. Notably, for each dataset-class pair, we use a single source image for the proxy training phase, and compute a single g-direction. We highlight that g-directions are in fact global, as indicated by their Flip Rate (FR) – percentage of images for which the classifier’s decision was flipped – being close to 100%.

On CelebA-HQ, we outperform current SOTA black-box method TiME in 6 out of 8 metrics for both smile and age classes. Note that, unlike TiME, we do not assume classifier’s training data availability in this case, as we use DiffAE trained on FFHQ-256. This assumption lies at the core of the TiME method, as they require distilling the knowledge from the training dataset. On the contrary, for CelebA-HQ, we only require a single image for the proxy. Notably, we also use a much smaller model (about 6 times less parameters), as TiME is based on Stable Diffusion V1.4 [1], a large text-to-image foundation model. We achieve such performance while using only a single direction. We are also able to compete with white-box methods despite a natural disadvantage. For the age class, we outperform all methods on sFID,

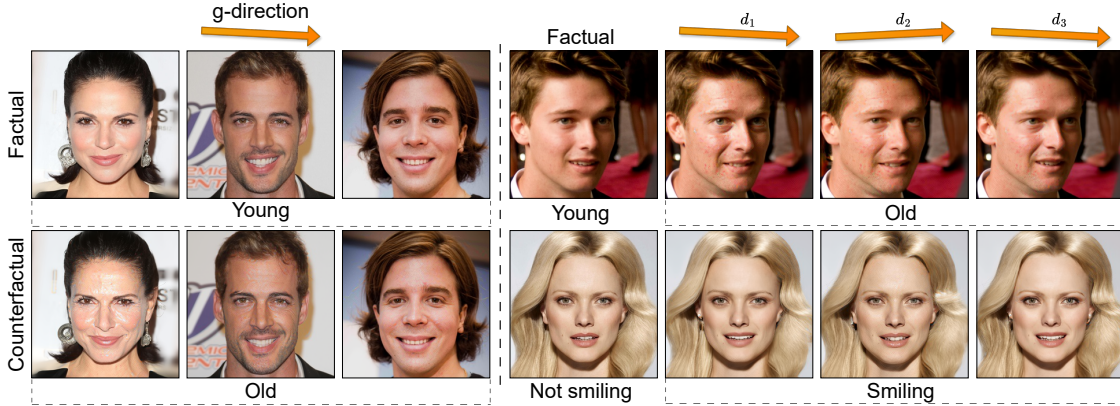


Figure 2: (Left) Factual (top) and counterfactual (bottom) images from a single g-direction for age class on CelebA-HQ. Semantic changes vary from image to image. (Right) Influence of g-directions resulting from different source images for age (top) and smile (bottom). Due to different semantic changes, they can act alone as source of diversity.

FS and CD, take second place in FID and FR, and are worse than only ACE on FVA. For the smile class, we score the highest FR and smallest sFID, once again being worse than only ACE on FVA and FS. For both classes, we outperform all non-DM based methods in every available metric.

As TiME does not evaluate on CelebA, we compare to white-box methods only. Despite being black-box, we achieve a competitive performance. In terms of DM-based approaches, for the smile class, we beat all methods on FS and MNAC, tie the best performance for FVA and score second on FR. For the age class, we beat all methods except ACE on FVA, FS and CD. Once again, we outperform non-DM based methods in every available metric.

In 2, we show that the properties of g-directions are transferable to real-world use-cases by evaluating the CEs obtained on CheXpert validation set for 5 different classes. A high S^3 metric indicates that the obtained CEs closely resemble the original images while flipping the classifier’s decision. In 3 cases, our g-directions achieve FR of about 90%, hence preserving the globality property. For 2 other diseases, we see a slight decrease in FR. However, CEs are still obtained for over 70% of images. For visual examples of explanations, please refer to the Appendix.

To assess the influence of the source image on the resulting g-direction, we perform an ablation study. For the age class on CelebA-HQ, we choose arbitrary 5 source images, train the proxy on each of them independently and generate CEs on 128 images using the g-directions. We include the mean and standard deviation of each metric in 3. Importantly, we observe little variation in the obtained FR, indicating that each image results in a g-direction that is indeed global. Mean values of other metrics achieve values similar to those shown in 1, with little variation. These results indicate that the choice of the source image has minimal influence on CEs from a quantitative point of view.

We also assess the CEs obtained with g-directions qualitatively. In 2 (left), we show explanations obtained with a single g-direction on the age class from CelebA-HQ. Interestingly, it is difficult to indicate a single attribute that this direction influences in every image. For the woman on the left, it changes the skin and mouth area, while for the man in the middle and on the right it focuses on the upper lip. While the changes on the woman’s face agree with the intuition about what should influence the classifier’s decision, we find it surprising that changing the upper lip area for men has the same result. This could be explained by the presence of moustache on the images of older people which should be a good indicator of the age attribute. To further interpret a single g-direction, we compute the absolute difference between the original image and its CE, and average them across a set of images. We include the resulting maps for both CelebA-HQ classes in 4. The age g-direction seems to mostly focus on the eyebrows, the mouth area and the left side of the chin, with the smile direction being much more focused on lips/teeth. We also compare the CEs obtained for the same image with g-directions from different source images for the age class. In 2 (right), we observe that the resulting

Table 2: Evaluation of g-directions on CheXpert dataset. Rows indicate results for a specific class (disease) using a single g-direction, columns indicate the used metric.

Class \ Metric	$S^3(\uparrow)$	COUT(\uparrow)	FR(\uparrow)
Pleural effusion	0.7863	0.4126	91.1
Lung opacity	0.8430	0.2171	91.4
Support devices	0.8247	0.2321	89.4
Lung lesion	0.7812	0.2030	74.7
Atelectasis	0.8760	0.2013	78.3

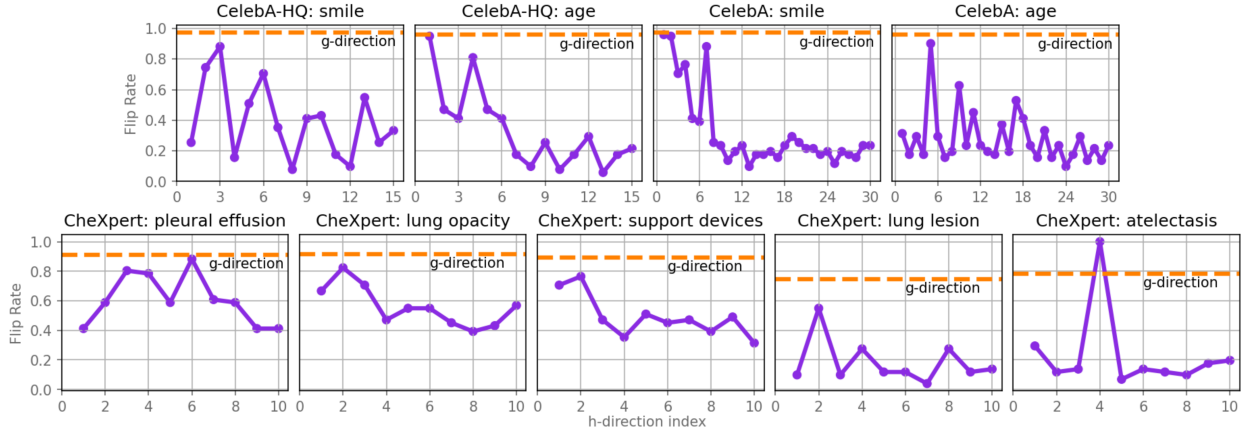


Figure 3: Globality of the h-directions. For each dataset-class pair, FR of each direction on a set of 128 images is plotted. The behavior varies across all considered cases.

directions differ significantly in how they influence the image to change the classifier’s decision. For example, for the age class, each of them modifies the skin in some way and has different effect on the person’s eyes and chin. Assuming that a set of images is available to be used as source images, g-directions can therefore act alone as source of diversity.

5.2 Evaluation of h-directions

We proceed with an analysis of the h-directions, considered mainly as a tool for diversifying the CEs in case one wants to obtain more than a single explanation, which is the inherent drawback of a single g-direction.

At first, we assess the h-directions from the point of globality. For each dataset-class pair, we select the top h-directions, generate CEs using each of them on a set of 128 images and compute their FR. The results can be observed in 3. Interestingly, in almost every case, there are at least a few h-directions that achieve FR very close to the corresponding g-direction. The relationship between FR and the h-direction’s index number varies across datasets and classes. For smile on CelebA-HQ and age on CelebA, it oscillates between low and high values with a tendency of decreasing. For age on CelebA-HQ and smile on CelebA, the first directions reach the highest FR, which then gradually decreases. Interestingly, on CheXpert, FR seems to be approximately constant. There is also a single exception, the atelectasis class on CheXpert, where the 4th h-direction achieves significantly higher FR than the g-direction.

To further assess their performance, we choose top 3 h-directions (in terms of FR) for smile on CelebA-HQ and generate additional CEs to compare them with g-directions. The resulting metrics are shown in 4. We observe that they perform comparably with the g-direction from 1. It is also possible to match the performance of the top 3 by combining the remaining 12 directions. Specifically, for each image, we choose its CE from all explanations generated with these directions by picking the one with the lowest CF loss. As indicated by 4, this strategy allows for achieving very similar results to the top 3. For extended quantitative results on other datasets and classes, see Appendix.

In 4, we observe that the orthogonality of the h-directions translates to different semantic changes in the obtained CEs. For the smile class, each direction modifies the cheeks and mouth area differently. For the age class, each direction has different effect on the skin tone, eyes and the type of glasses. We include more visual examples for all datasets in the Appendix.

5.3 Understanding counterfactual explanations

Black-box methods for generating CEs are prone to introducing irrelevant changes in the image since they use a much weaker signal from the classifier than white-box approaches. This limits the effectiveness of the obtained CEs in showing which changes were particularly important for the model’s decision. With BB-LIG, GCDs are inherently capable of generating attribution maps that highlight more important regions and downweigh those of smaller relevance.

Table 3: Ablation study regarding the choice of the source image and the resulting g-directions for age on CelebA-HQ. Mean ± standard deviation is reported. Each metric was computed using a set of 128 images and then averaged over 5 source images.

FVA(↑)	FS(↑)	MNAC(↓)	CD(↓)	COUT(↑)	FR(↑)
98.84 ± 0.3	0.7728 ± 0.028	4.22 ± 0.36	3.99 ± 0.35	0.2626 ± 0.0281	96.4 ± 0.8

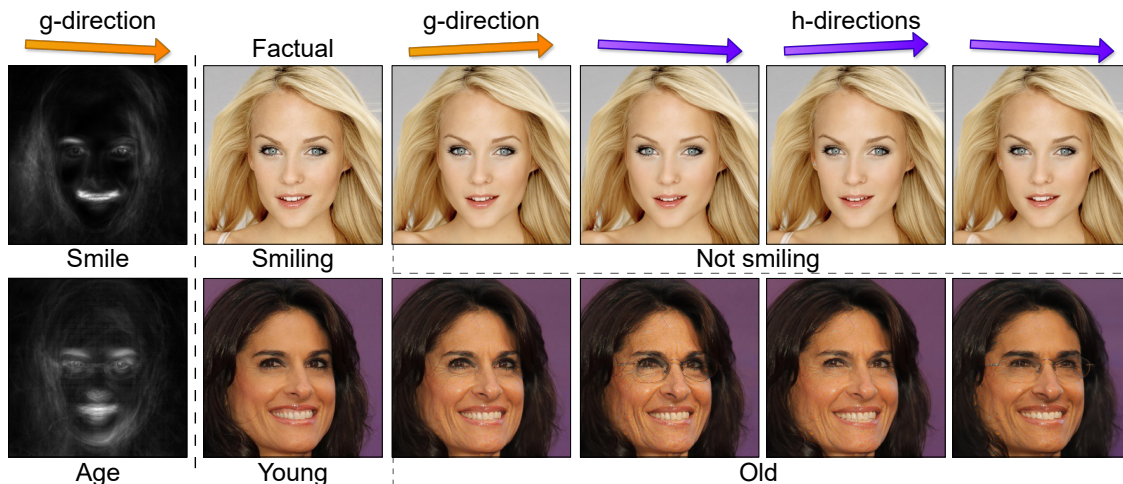


Figure 4: (Left) *g*-directions can be interpreted by computing mean absolute difference between original image and its CE over a set of images. (Right) While *g*-directions lead to only single counterfactual per image, we may obtain more explanations by exploiting the *h*-directions. Their orthogonality in the semantic latent space results in producing diverse explanations.

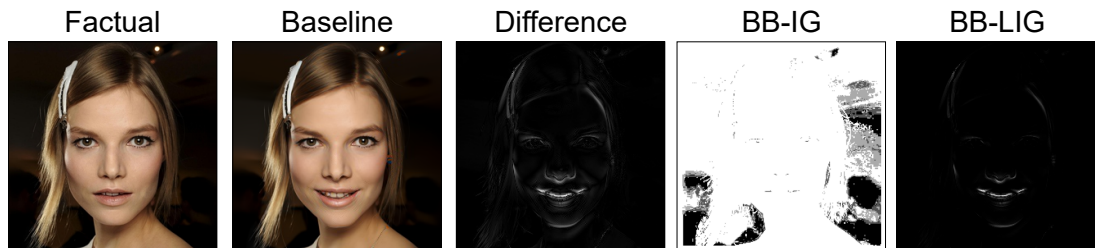


Figure 5: Understanding of the most important changes in CEs. We obtain the *baseline* from the *factual* image by moving along a GCD to the point where the classifier’s predicted probability equals approximately 0. *Difference* denotes the absolute difference between factual and baseline images. *BB-IG* results from using IG with finite-difference method and interpolating between the factual image and a black baseline. *BB-LIG* shows much more detailed attributions obtained with our method.

Simultaneously, BB-LIG can act as a standalone black-box attribution method, since it allows the user to understand which features the classifier’s pays attention to.

In 5, we include example factual image and a baseline obtained with GCD, which is a CE with the classifier’s output being approximately 0. Visual comparison of the original and baseline images suggests that only the mouth area was influenced by GCD. By computing the absolute difference between them, we also observe that some changes were introduced to the hair clip, eyes and nose. As we assume only black-box access to the classifier, directly computing the gradient is not possible which prevents the use of standard IG neither for the original nor for the CE. We can resort to using the finite difference method with a black image as baseline (BB-IG) to compare the resulting attribution maps for the factual image and our CE. However, as shown in 5, this type of approximation results in meaningless attribution map, suggesting that standard IG cannot be easily converted to a black-box method. These issues are mitigated by BB-LIG which acts as a weighing mechanism for the introduced changes by assigning higher attributions to regions relevant to the black-box classifier. As we can see, it greatly emphasizes the teeth and the tip of the nose, and assigns almost zero attributions to other modified areas. We include more visual examples of BB-LIG in the Appendix.

Table 4: Evaluation of top 3 *h*-directions (in terms of Flip Rate) and a combination of other 12 on the smile class from CelebA-HQ. Rows indicate results for each direction.

h-direction \ Metric	FID(↓)	sFID(↓)	FVA(↑)	FS(↑)	MNAC(↓)	CD(↓)	COUT(↑)	FR(↑)
1st	8.27	9.11	99.0	0.8247	3.47	3.69	0.4102	91.4
2nd	8.14	8.92	91.1	0.7333	3.65	4.13	0.3730	78.1
3rd	9.34	9.52	97.6	0.7635	3.66	4.03	0.3945	72.7
Others combined	8.84	9.54	99.0	0.8208	3.41	4.22	0.3641	94.1

6 Conclusions

Our motivation for applying DiffAE to the task of generating CEs sparks from a simple question: if global editing directions, responsible for specific concepts, can be discovered in DiffAE’s semantic latent space, does this space also possess global directions responsible for the decision of a specific classifier for every image? We give a positive answer to this question and empirically explain its profound consequences. We show a strong relationship between the emergent capabilities of generative modelling and supervised learning objectives which serves as a purpose for further exploration of DMs in generating CEs for black-box models. The introduced proxy-based approach can be easily adapted to other generative models that possess rich, low-dimensional representations. Future research could also further address the topic of assigning attributions to modifications introduced to produce CEs as to obtain a better understanding of the classifier and its decision-making process.

References

- [1] Robin Rombach, Andreas Blattmann, Dominik Lorenz, Patrick Esser, and Björn Ommer. High-resolution image synthesis with latent diffusion models. In *Proceedings of the IEEE/CVF conference on computer vision and pattern recognition*, pages 10684–10695, 2022.
- [2] David Silver, Aja Huang, Chris J Maddison, Arthur Guez, Laurent Sifre, George Van Den Driessche, Julian Schrittwieser, Ioannis Antonoglou, Veda Panneershelvam, Marc Lanctot, et al. Mastering the game of go with deep neural networks and tree search. *nature*, 529(7587):484–489, 2016.
- [3] Yukun Zhou, Mark A Chia, Siegfried K Wagner, Murat S Ayhan, Dominic J Williamson, Robbert R Struyven, Timing Liu, Moucheng Xu, Mateo G Lozano, Peter Woodward-Court, et al. A foundation model for generalizable disease detection from retinal images. *Nature*, pages 1–8, 2023.
- [4] Maciej A. Mazurowski, Haoyu Dong, Hanxue Gu, Jichen Yang, Nicholas Konz, and Yixin Zhang. Segment anything model for medical image analysis: An experimental study. *Medical Image Analysis*, 89:102918, 2023.
- [5] Claudine Badue, Rânik Guidolini, Raphael Vivacqua Carneiro, Pedro Azevedo, Vinicius B Cardoso, Avelino Forechi, Luan Jesus, Rodrigo Berriel, Thiago M Paixao, Filipe Mutz, et al. Self-driving cars: A survey. *Expert Systems with Applications*, 165:113816, 2021.
- [6] Hugo Touvron, Louis Martin, Kevin Stone, Peter Albert, Amjad Almahairi, Yasmine Babaei, Nikolay Bashlykov, Soumya Batra, Prajjwal Bhargava, Shruti Bhosale, et al. Llama 2: Open foundation and fine-tuned chat models. *arXiv preprint arXiv:2307.09288*, 2023.
- [7] Andreas Holzinger, Anna Saranti, Christoph Molnar, Przemyslaw Biecek, and Wojciech Samek. Explainable ai methods-a brief overview. In *International Workshop on Extending Explainable AI Beyond Deep Models and Classifiers*, pages 13–38. Springer, 2020.
- [8] Ramaravind K Mothilal, Amit Sharma, and Chenhao Tan. Explaining machine learning classifiers through diverse counterfactual explanations. In *Proceedings of the 2020 Conference on Fairness, Accountability, and Transparency*, pages 607–617, 2020.
- [9] S Wachter, B Mittelstadt, and C Russell. Counterfactual explanations without opening the black box: automated decisions and the gdpr. *Harvard Journal of Law and Technology*, 31(2):841–887, 2018.
- [10] Judea Pearl. Causal inference in statistics: An overview. *Statistics Surveys*, 3(none):96 – 146, 2009.
- [11] Yash Goyal, Ziyang Wu, Jan Ernst, Dhruv Batra, Devi Parikh, and Stefan Lee. Counterfactual visual explanations. In Kamalika Chaudhuri and Ruslan Salakhutdinov, editors, *Proceedings of the 36th International Conference on Machine Learning*, volume 97 of *Proceedings of Machine Learning Research*, pages 2376–2384. PMLR, 09–15 Jun 2019.
- [12] Ilia Stepin, Jose M. Alonso, Alejandro Catala, and Martín Pereira-Fariña. A survey of contrastive and counterfactual explanation generation methods for explainable artificial intelligence. *IEEE Access*, 9:11974–12001, 2021.
- [13] Guillaume Jeanneret, Loïc Simon, and Frédéric Jurie. Adversarial counterfactual visual explanations. In *Proceedings of the IEEE/CVF Conference on Computer Vision and Pattern Recognition*, pages 16425–16435, 2023.
- [14] Guillaume Jeanneret, Loïc Simon, and Frédéric Jurie. Diffusion models for counterfactual explanations. In *Proceedings of the Asian Conference on Computer Vision*, pages 858–876, 2022.
- [15] Maximilian Augustin, Valentyn Boreiko, Francesco Croce, and Matthias Hein. Diffusion visual counterfactual explanations. *Advances in Neural Information Processing Systems*, 35:364–377, 2022.

- [16] K. Farid et al. Latent diffusion counterfactual explanations. *arXiv*, 2023.
- [17] Jascha Sohl-Dickstein, Eric Weiss, Niru Maheswaranathan, and Surya Ganguli. Deep unsupervised learning using nonequilibrium thermodynamics. In Francis Bach and David Blei, editors, *Proceedings of the 32nd International Conference on Machine Learning*, volume 37 of *Proceedings of Machine Learning Research*, pages 2256–2265. PMLR, 2015.
- [18] Jonathan Ho, Ajay Jain, and Pieter Abbeel. Denoising diffusion probabilistic models. In H. Larochelle, M. Ranzato, R. Hadsell, M.F. Balcan, and H. Lin, editors, *Advances in Neural Information Processing Systems*, volume 33, 2020.
- [19] Yang Song, Jascha Sohl-Dickstein, Diederik P Kingma, Abhishek Kumar, Stefano Ermon, and Ben Poole. Score-based generative modeling through stochastic differential equations. In *International Conference on Learning Representations*, 2021.
- [20] Guillaume Jeanneret, Loïc Simon, and Frédéric Jurie. Text-to-image models for counterfactual explanations: a black-box approach. In *Proceedings of the IEEE/CVF Winter Conference on Applications of Computer Vision*, pages 4757–4767, 2024.
- [21] O. Lang et al. Explaining in style: Training a gan to explain a classifier in stylespace. *ICCV*, 2021.
- [22] Ian J Goodfellow, Jonathon Shlens, and Christian Szegedy. Explaining and harnessing adversarial examples. *arXiv preprint arXiv:1412.6572*, 2014.
- [23] Christian Szegedy, Wojciech Zaremba, Ilya Sutskever, Joan Bruna, Dumitru Erhan, Ian J. Goodfellow, and Rob Fergus. Intriguing properties of neural networks. In Yoshua Bengio and Yann LeCun, editors, *2nd International Conference on Learning Representations, ICLR 2014, Banff, AB, Canada, April 14-16, 2014, Conference Track Proceedings*, 2014.
- [24] Arnaud Van Looveren and Janis Klaise. Interpretable counterfactual explanations guided by prototypes. In *Joint European Conference on Machine Learning and Knowledge Discovery in Databases*, pages 650–665. Springer, 2021.
- [25] Jayaraman Thiagarajan, Vivek Sivaraman Narayanaswamy, Deepta Rajan, Jia Liang, Akshay Chaudhari, and Andreas Spanias. Designing counterfactual generators using deep model inversion. *Advances in Neural Information Processing Systems*, 34:16873–16884, 2021.
- [26] Frederik Hvilshoj, Alexandros Iosifidis, and Ira Assent. Ecinn: efficient counterfactuals from invertible neural networks. *arXiv preprint arXiv:2103.13701*, 2021.
- [27] Valentyn Boreiko, Maximilian Augustin, Francesco Croce, Philipp Berens, and Matthias Hein. Sparse visual counterfactual explanations in image space. In *DAGM German Conference on Pattern Recognition*, pages 133–148. Springer, 2022.
- [28] Lisa Schut, Oscar Key, Rory Mc Grath, Luca Costabello, Bogdan Sacaleanu, Yarin Gal, et al. Generating interpretable counterfactual explanations by implicit minimisation of epistemic and aleatoric uncertainties. In *International Conference on Artificial Intelligence and Statistics*, pages 1756–1764. PMLR, 2021.
- [29] Diederik P Kingma and Max Welling. Auto-encoding variational bayes. *arXiv preprint arXiv:1312.6114*, 2013.
- [30] Ian Goodfellow, Jean Pouget-Abadie, Mehdi Mirza, Bing Xu, David Warde-Farley, Sherjil Ozair, Aaron Courville, and Yoshua Bengio. Generative adversarial nets. *Advances in neural information processing systems*, 27, 2014.
- [31] Sumedha Singla, Brian Pollack, Junxiang Chen, and Kayhan Batmanghelich. Explanation by progressive exaggeration. *arXiv preprint arXiv:1911.00483*, 2019.
- [32] Saeed Khorrarn and Li Fuxin. Cycle-consistent counterfactuals by latent transformations. In *Proceedings of the IEEE/CVF Conference on Computer Vision and Pattern Recognition*, pages 10203–10212, 2022.
- [33] Pau Rodríguez, Massimo Caccia, Alexandre Lacoste, Lee Zamparo, Issam Laradji, Laurent Charlin, and David Vazquez. Beyond trivial counterfactual explanations with diverse valuable explanations. In *Proceedings of the IEEE/CVF International Conference on Computer Vision*, pages 1056–1065, 2021.
- [34] Paul Jacob, Éloi Zablocki, Hedi Ben-Younes, Mickaël Chen, Patrick Pérez, and Matthieu Cord. Steex: steering counterfactual explanations with semantics. In *European Conference on Computer Vision*, pages 387–403. Springer, 2022.
- [35] Sheng-Min Shih, Pin-Ju Tien, and Zohar Karnin. Ganmex: One-vs-one attributions using gan-based model explainability. In *International Conference on Machine Learning*, pages 9592–9602. PMLR, 2021.
- [36] Zhengli Zhao, Dheeru Dua, and Sameer Singh. Generating natural adversarial examples. *arXiv preprint arXiv:1710.11342*, 2017.

- [37] Nina Weng, Paraskevas Pegios, Aasa Feragen, Eike Petersen, and Siavash Bigdeli. Fast diffusion-based counterfactuals for shortcut removal and generation. *arXiv*, 2023.
- [38] J. Vendrow et al. Dataset interfaces: Diagnosing model failures using controllable counterfactual generation. *arXiv*, 2023.
- [39] V. Prabhu et al. LANCE: Stress-testing visual models by generating language-guided counterfactual images. *NeurIPS*, 2023.
- [40] Viraj Uday Prabhu, David Acuna, Rafid Mahmood, Marc T. Law, Yuan-Hong Liao, Judy Hoffman, Sanja Fidler, and James Lucas. Bridging the sim2real gap with CARE: Supervised detection adaptation with conditional alignment and reweighting. *Transactions on Machine Learning Research*, 2023.
- [41] Kwon M. et al. Diffusion models already have a semantic latent space. *ICLR*, 2023.
- [42] R. Hass et al. Discovering interpretable directions in the semantic latent space of diffusion models. *arXiv*, 2023.
- [43] Y. Park et al. Understanding the latent space of diffusion models through the lens of riemannian geometry. *NeurIPS*, 2023.
- [44] Qiucheng Wu, Yujian Liu, Handong Zhao, Ajinkya Kale, Trung Bui, Tong Yu, Zhe Lin, Yang Zhang, and Shiyu Chang. Uncovering the disentanglement capability in text-to-image diffusion models. In *Proceedings of the IEEE/CVF Conference on Computer Vision and Pattern Recognition (CVPR)*, pages 1900–1910, June 2023.
- [45] Jaeseok Jeong, Mingi Kwon, and Youngjung Uh. Training-free content injection using h-space in diffusion models. In *Proceedings of the IEEE/CVF Winter Conference on Applications of Computer Vision (WACV)*, pages 5151–5161, January 2024.
- [46] Zihao Wang, Lin Gui, Jeffrey Negrea, and Victor Veitch. Concept algebra for (score-based) text-controlled generative models. In A. Oh, T. Neumann, A. Globerson, K. Saenko, M. Hardt, and S. Levine, editors, *Advances in Neural Information Processing Systems*, volume 36, pages 35331–35349. Curran Associates, Inc., 2023.
- [47] Konpat Preechakul, Nattanat Chatthee, Suttisak Wizadwongsa, and Supasorn Suwajanakorn. Diffusion autoencoders: Toward a meaningful and decodable representation. In *Proceedings of the IEEE/CVF Conference on Computer Vision and Pattern Recognition*, pages 10619–10629, 2022.
- [48] Yoshua Bengio, Aaron Courville, and Pascal Vincent. Representation learning: A review and new perspectives. *IEEE transactions on pattern analysis and machine intelligence*, 35(8):1798–1828, 2013.
- [49] Ting Chen, Simon Kornblith, Mohammad Norouzi, and Geoffrey Hinton. A simple framework for contrastive learning of visual representations. In *International conference on machine learning*, pages 1597–1607. PMLR, 2020.
- [50] Karen Simonyan, Andrea Vedaldi, and Andrew Zisserman. Deep inside convolutional networks: Visualising image classification models and saliency maps, 2014.
- [51] Avanti Shrikumar, Peyton Greenside, and Anshul Kundaje. Learning important features through propagating activation differences. In *International conference on machine learning*, pages 3145–3153. PMLR, 2017.
- [52] Sebastian Bach, Alexander Binder, Grégoire Montavon, Frederick Klauschen, Klaus-Robert Müller, and Wojciech Samek. On pixel-wise explanations for non-linear classifier decisions by layer-wise relevance propagation. *PLoS one*, 10(7):e0130140, 2015.
- [53] Luca Longo, Mario Brcic, Federico Cabitza, Jaesik Choi, Roberto Confalonieri, Javier Del Ser, Riccardo Guidotti, Yoichi Hayashi, Francisco Herrera, Andreas Holzinger, Richard Jiang, Hassan Khosravi, Freddy Lecue, Gianclaudio Malgieri, Andrés Páez, Wojciech Samek, Johannes Schneider, Timo Speith, and Simone Stumpf. Explainable artificial intelligence (xai) 2.0: A manifesto of open challenges and interdisciplinary research directions. *Information Fusion*, 106:102301, June 2024.
- [54] Mukund Sundararajan, Ankur Taly, and Qiqi Yan. Axiomatic attribution for deep networks. In *International conference on machine learning*, pages 3319–3328. PMLR, 2017.
- [55] Daniel D Lundstrom, Tianjian Huang, and Meisam Razaviyayn. A rigorous study of integrated gradients method and extensions to internal neuron attributions. In *International Conference on Machine Learning*, pages 14485–14508. PMLR, 2022.
- [56] Pascal Sturmfels, Scott Lundberg, and Su-In Lee. Visualizing the impact of feature attribution baselines. *Distill*, 2020. <https://distill.pub/2020/attribution-baselines>.
- [57] Samuele Poppi, Marcella Cornia, Lorenzo Baraldi, and Rita Cucchiara. Revisiting the evaluation of class activation mapping for explainability: A novel metric and experimental analysis. In *Proceedings of the IEEE/CVF Conference on Computer Vision and Pattern Recognition*, pages 2299–2304, 2021.

- [58] Amil Dravid, Florian Schiffrers, Boqing Gong, and Aggelos K. Katsaggelos. medxgan: Visual explanations for medical classifiers through a generative latent space. In *Proceedings of the IEEE/CVF Conference on Computer Vision and Pattern Recognition (CVPR) Workshops*, pages 2936–2945, June 2022.
- [59] Richard Zhang, Phillip Isola, Alexei A Efros, Eli Shechtman, and Oliver Wang. The unreasonable effectiveness of deep features as a perceptual metric. In *CVPR*, 2018.
- [60] Prafulla Dhariwal and Alexander Nichol. Diffusion models beat gans on image synthesis. *Advances in neural information processing systems*, 34:8780–8794, 2021.
- [61] Olaf Ronneberger, Philipp Fischer, and Thomas Brox. Convolutional networks for biomedical image segmentation. In *Medical Image Computing and Computer-Assisted Intervention–MICCAI 2015 Conference Proceedings*, 2022.
- [62] Jiaming Song, Chenlin Meng, and Stefano Ermon. Denoising diffusion implicit models. In *International Conference on Learning Representations*, 2021.
- [63] Pei-bai Zhou. Finite difference method. *Numerical Analysis of Electromagnetic Fields*, 1993.
- [64] Ziwei Liu, Ping Luo, Xiaogang Wang, and Xiaoou Tang. Deep learning face attributes in the wild. In *Proceedings of International Conference on Computer Vision (ICCV)*, December 2015.
- [65] Tero Karras, Timo Aila, Samuli Laine, and Jaakko Lehtinen. Progressive growing of gans for improved quality, stability, and variation. In *International Conference on Learning Representations*, 2017.
- [66] Gao Huang, Zhuang Liu, Laurens Van Der Maaten, and Kilian Q Weinberger. Densely connected convolutional networks. In *Proceedings of the IEEE conference on computer vision and pattern recognition*, pages 4700–4708, 2017.
- [67] Jeremy Irvin, Pranav Rajpurkar, Michael Ko, Yifan Yu, Silvana Ciurea-Ilicus, Chris Chute, Henrik Marklund, Behzad Haghgoo, Robyn Ball, Katie Shpanskaya, et al. Chexpert: A large chest radiograph dataset with uncertainty labels and expert comparison. In *Proceedings of the AAAI conference on artificial intelligence*, volume 33, pages 590–597, 2019.
- [68] Hubert Baniecki, Maciej Chrabaszcz, Andreas Holzinger, Bastian Pfeifer, Anna Saranti, and Przemyslaw Biecek. Be careful when evaluating explanations regarding ground truth. *arXiv preprint arXiv:2311.04813*, 2023.
- [69] T. Karras, S. Laine, and T. Aila. A style-based generator architecture for generative adversarial networks. In *IEEE Transactions on Pattern Analysis & Machine Intelligence*, 2021.